Femtosecond pulse propagation in nitrogen: Numerical study of (3+1)-dimensional extended nonlinear Schrödinger equation with shock-term correction

Taro Ando* and Masatoshi Fujimoto
Hamamatsu Photonics K.K., Central Research Laboratory, Hirakuchi, Hamakita-City, Shizuoka, 434-8601, Japan
(Received 14 September 2004; revised manuscript received 30 March 2005; published 31 August 2005)

We develop an accurate and efficient method for calculating evolution due to the extended nonlinear Schrödinger equation, which describes the propagation behavior of a femtosecond light pulse in a nonlinear medium. Applying Suzuki's exponential operator expansion to the evolution operator based on the finite-differential formulation, we realize the accurate and fast calculation that can be performed without large-scale computing systems even for (3+1)-dimensional problems. To study the correspondence between experiments and calculations, we calculate the propagation behavior of a femtosecond light pulse that is weakly focused in nitrogen gas of various pressures and compare the calculation results to the experimental ones. The calculation results reproduce the relative behavior of the spatial light pattern observed during the propagation. Additionally, the multiple-cone formation and interaction between two collimated pulses in nitrogen gas are also demonstrated as applications of the developed method.

DOI: 10.1103/PhysRevE.72.026706 PACS number(s): 02.70.−c, 42.25.Bs, 42.65.−k, 52.38.Hb

I. INTRODUCTION

The propagation phenomenon of an ultrashort light pulse has become an issue of interest in both fundamental and applied physics. The development of femtosecond laser apparatus has brought a suitable light source for the experimental study of the high-power regime of input light pulses, and the results contain fruitful information on plasma and nonlinear physics [1–7], such as the self-focusing, self-phase modulation, plasma defocusing, and so on. With advances in experimental research, numerical studies have also become significant for tracing the origin of observed phenomena [1,2,7]. However, the numerical results of pulse propagation are not directly validated because the instantaneous observation of the propagating light pulse has not been realized in experiments to date. Recently, a measurement technique, femtosecond time-resolved optical polarigraphy (FTOP) [8–11], was developed to directly observe the spatial pattern of propagating femtosecond light pulses at each moment. The result is that FTOP enables direct comparison between experiments and calculations.

At the beginning of the theoretical studies, the nonlinear Schrödinger equation (NLSE) was adopted as a simple model of propagating light pulses [12]. The NLSE, based upon the assumption of slowly varying envelope approximation (SVEA), is a good model for a picosecond light pulse; however, it fails in the femtosecond regime due to the rapid change in an envelope of the femtosecond light pulse. To correct this deviation, modified NLSE (MNLSE) has been proposed that includes a time derivative of the pulse envelope [13,14], which is further developed to the extended NLSE (ENLSE) with plasma defocusing effects. The ENLSE is a modern standard model for femtosecond light propagation in gases [2–7]. Also, more recently, the importance of a correction beyond SVEA has been highlighted for reproducing the light behavior of less than several monocycles [15–19].

Because analytical solutions for NLSEs are not available, numerical methods play significant roles. To solve the complicated NLSEs accurately, various methods have been established, i.e., the Clank-Nicholson method, the alternating directional implicit method, the split-step Fourier method (SSF) [20], etc. Among these methods, SSF is one of the most efficient ones and often used as a solver for general NLSEs. For example, the multiple-cone structure of an intense femtosecond light pulse in silica is observed and analyzed by applying the SSF to the (2+1)-dimensional [(2+1)D] ENLSE beyond SVEA [21,22]. Furthermore, the multiple filamentation of a high-power laser pulse in the air is also investigated with (3+1)-dimensional [(3+1)D] ENLSE [2]. Besides the existence of such extensive works, further development of the calculation method, which can be applied to the (3+1)D ENLSE beyond SVEA, is required in order to study spatially asymmetrical propagation of ultrafast light pulses.

In this paper, we develop an efficient and accurate method for numerically solving (3+1)D ENLSE beyond SVEA. Our method is based on Suzuki's exponential-product expansion (EPE) [23–26] with the finite difference treatment of the real space time [27,28]. This approach is an extension of that in Ref. [30] for the treatment of the third-order differential operator that arises from the shock-term correction. Consequently, the method is accurate, efficient with $O(N)$ calculation steps, and also suitable for parallel computing. The typical elapsed time is about 11 h for calculating 1400 evolution steps of $384\times384\times384$ data. As a demonstration of the method, we apply it to the propagation phenomena of femtosecond light pulses that are weakly focused in nitrogen (N_2) gas at various pressures. Our calculation reproduces experimental results [10] about the relative change of propagation behavior in various N_2 pressures. As examples of nonsymmetrical (3+1)D pulse propagation, multiple-cone formation and interaction of two collimated pulses are also demonstrated.

*Corresponding author. Electronic address: taro@crl.hpk.co.jp

The remainder of this paper is organized as follows. In Sec. II, we formulate an accurate and efficient computational scheme for integrating ENLSE. Calculation results on the propagation phenomena of a femtosecond laser pulse in nitrogen gas are shown and compared with the experimental results in Sec. III. In addition, two characteristic pulse propagation phenomena in nitrogen gas are also demonstrated, i.e., the multiple-cone formation and interaction between two pulses. Finally, the results and discussions are summarized in Sec. IV.

II. CALCULATION METHOD

In this section, we formulate a numerical method for calculating propagation phenomena of femtosecond light pulses. The formulation is performed on MNLSE (not ENLSE) for the time being, and a plasma effect is introduced as a modification in Sec. II C.

When a femtosecond light pulse propagates into the z direction with a group velocity V_g, an electric-field envelope of the pulse, $\phi(\boldsymbol{r},\tau)$, obeys the following MNLSE beyond SVEA in a reference frame traveling at V_g:

$$\begin{aligned} i\frac{\partial}{\partial z}\phi(\boldsymbol{r},\tau) &= \hat{H}\phi(\boldsymbol{r},\tau) \\ &= \left[-\frac{\beta_2}{2}\left(-\frac{\partial^2}{\partial\tau^2}\right) + \frac{1}{2k_0n_0}\left(1-\frac{i}{\omega_0}\frac{\partial}{\partial\tau}\right)\left(-\frac{\partial^2}{\partial x^2}-\frac{\partial^2}{\partial y^2}\right)\right]\phi(\boldsymbol{r},\tau) \\ &\quad - n_2k_0\left(1+\frac{i}{\omega_0}\frac{\partial}{\partial\tau}\right)|\phi(\boldsymbol{r},\tau)|^2\phi(\boldsymbol{r},\tau). \end{aligned} \tag{1}$$

In Eq. (1), x and y denote the two-dimensional spatial position perpendicular to the z direction, whereas τ is a temporal variable on the co-moving frame with the light pulses and relates to the real time t as $\tau=t-z/V_g$. Moreover, n_0, n_2, β_2 are the refractive index, second-order nonlinear coefficient, and group velocity dispersion of the medium, respectively, while k_0 and ω_0 are the wave number and angular frequency of the incident light in the vacuum, respectively. The first-order partial differential operators with respect to τ in the right-hand side (rhs) of Eq. (1) correspond to the shock effects. Higher-order dispersion effects of the group velocity are ignored in Eq. (1), because they have little influence in dilute gas media. It is noted that the $|\phi|^2$-term in Eq. (1) should be recognized as an operator.

Once the envelope at a position z_0 in the z direction, $\phi_0(x,y,z_0,\tau)$, is given, we can numerically calculate evolution with the following formula for a sufficiently small evolution step, $\Delta z[=(z-z_0)/n]$:

$$\begin{aligned} \phi(x,y,z,\tau) &\approx \left[\exp\left(-i\frac{z-z_0}{n}\hat{H}\right)\right]^n\phi(x,y,z_0,\tau) \\ &= [\exp(-i\Delta z\hat{H})]^n\phi_0(x,y,\tau), \end{aligned} \tag{2}$$

where the initial envelope, $\phi(x,y,z_0,\tau)$, is denoted as $\phi_0(x,y,\tau)$ to clearly grasp its functional dependency on the variables. It is noted that the role of z and τ are interchanged in Eq. (1) compared to the familiar Schrödinger equation in quantum mechanics. Thus Eq. (2) means that the solution of Eq. (1) is given by calculating the z evolution of $\phi_0(x,y,\tau)$ step by step.

To numerically calculate the evolution according to Eq. (2), $\phi(x,y,\tau)$ is discretized to a set of complex values on $(2+1)$-dimensional lattice points with equal intervals, i.e., $\{\phi_{ika}\}$, following the finite-differential treatment. Here, we denote the intervals of lattice points in the x, y, and τ directions as Δx, Δy, and $\Delta\tau$, respectively, and label each lattice point with a set of integer numbers (i,k,a), where i and k label a position in the xy plane, while a does so in the τ direction ($i=0,1,\cdots,N_x-1$, $k=0,1,\cdots,N_y-1$, and $a=0,1,\cdots,N_\tau-1$, where N_α is a number of the points in the α direction). Based on the discretization of the real space time, we apply Suzuki's EPE to the evolution operator, $e^{-i\Delta z\hat{H}}$, and reduce it to a product of matrices that act on $\{\phi_{ika}\}$.

The procedural essence of EPE is to decompose the total evolution operator into a product of partial evolution operators. Suppose that the total Hamiltonian is given as $\hat{H}=\hat{H}_1+\hat{H}_2+\cdots+\hat{H}_N$ and that each $\hat{H}_i$ depends on z only through ϕ. In this case, the following EPE formula is known, which is correct up to the order of $O(\Delta z^2)$ [23–28]:

$$\begin{aligned} e^{i\Delta z\hat{H}} &= e^{i\Delta z(\hat{H}_1+\hat{H}_2+\cdots+\hat{H}_N)} \\ &\approx e^{i\Delta z\hat{H}_N/2}\cdots e^{i\Delta z\hat{H}_2/2}e^{i\Delta z\hat{H}_1}\times e^{i\Delta z\hat{H}_2/2}\cdots e^{i\Delta z\hat{H}_N/2} \\ &\quad + O(\Delta z^2). \end{aligned} \tag{3}$$

This formula is referred to as a symmetrical decomposition formula of the second order and is especially useful when each partial evolution operator $e^{i\Delta z\hat{H}_i/2}$ can be calculated easily. Here, the important feature of EPE is that the unitarity of the evolution operator strictly holds in the decomposition. With Eq. (3), we can obtain an approximated expression of the total evolution operator, even when the exponential of $\hat{H}$ is difficult to calculate directly. Thus it is necessary to establish the explicit expressions of the partial evolution operators suitable for numerical computation.

To calculate the evolution according to Eq. (1) with the help of Eq. (3), we decompose the total Hamiltonian as follows:

$$\begin{aligned} \hat{H} &= -\frac{\beta_2}{2}\left(-\frac{\partial^2}{\partial\tau^2}\right) + \frac{1}{2k_0n_0}\left(-\frac{\partial^2}{\partial x^2}\right) + \frac{1}{2k_0n_0}\left(-\frac{\partial^2}{\partial y^2}\right) \\ &\quad - \frac{i}{2k_0n_0\omega_0}\left(-\frac{\partial}{\partial\tau}\frac{\partial^2}{\partial x^2}\right) - \frac{i}{2k_0n_0\omega_0}\left(-\frac{\partial}{\partial\tau}\frac{\partial^2}{\partial y^2}\right) \\ &\quad - \left(n_2k_0|\phi|^2 + i\frac{n_2k_0}{\omega_0}\frac{\partial|\phi|^2}{\partial\tau}\right) - i\frac{n_2k_0}{\omega_0}|\phi|^2\frac{\partial}{\partial\tau} \\ &= \hat{K}_{\tau\tau}+\hat{K}_{xx}+\hat{K}_{yy}+\hat{K}_{\tau xx}+\hat{K}_{\tau yy}+\hat{V}+\hat{V}_\tau, \end{aligned} \tag{4}$$

where $\hat{K}$ represents differential operators with respect to the variables indicated by subscripts, while $\hat{V}$ denotes a nonlinear interaction term including the Kerr effect. The residual

term $\hat{V}_\tau$ is a temporal differential operator arising from the shock-term correction of the Kerr nonlinear term.

To further develop the numerical procedure, discretized expressions of the operators are required. In this paper, we apply the lowest-order expression of the differential operator that acts on $\{\phi_{ik\alpha}\}$; for example,

$$\left(-\frac{\partial^2}{\partial x^2}\right)_{ij} = \frac{1}{(\Delta x)^2}\begin{pmatrix} 2 & -1 & 0 & \cdots & 0 \\ -1 & 2 & -1 & 0 & \vdots \\ 0 & -1 & 2 & \ddots & 0 \\ \vdots & 0 & \ddots & \ddots & -1 \\ 0 & \cdots & 0 & -1 & 2 \end{pmatrix}, \quad (5)$$

and

$$\left(\frac{\partial}{\partial \tau}\right)_{ab} = \frac{1}{2\Delta\tau}\begin{pmatrix} 0 & 1 & 0 & \cdots & 0 \\ -1 & 0 & 1 & 0 & \vdots \\ 0 & -1 & 0 & \ddots & 0 \\ \vdots & 0 & \ddots & \ddots & 1 \\ 0 & \cdots & 0 & -1 & 0 \end{pmatrix}, \quad (6)$$

where the matrix expression of $\partial^2/\partial x^2$ acts on the subscript of the x direction, j, while that of $\partial/\partial\tau$ acts on the subscript of the τ direction, b. The matrix expression of $\partial^2/\partial y^2$ is the same as Eq. (5), but the subscripts must be changed to those of the y direction, kl.

Using the discretized expression of Eq. (6), we can obtain the partial evolution operator due to the nonlinear interaction term ($\hat{V}$). It is noted that the operator $\hat{V}$ acts as a local multiplication of a position-dependent complex number. Therefore, the partial evolution operator $e^{-i\Delta z\hat{V}}$ works upon ϕ as

$$(e^{-i\Delta z\hat{V}}\phi)_{ika} = \exp\left[n_2 k_0 \Delta z\left(i|\phi_{ika}|^2 - \frac{|\phi|^{2\prime}_{ika}}{\omega_0}\right)\right]\phi_{ika} \quad (7)$$

in the discretized space time. In Eq. (7), the derivative of $|\phi|^2$ with respect to τ is defined as the following from Eq. (6):

$$|\phi|^{2\prime}_{ika} = \left.\frac{\partial|\phi|^2}{\partial\tau}\right|_{ika} = \frac{|\phi_{ik(a+1)}|^2 - |\phi_{ik(a-1)}|^2}{2\Delta\tau}. \quad (8)$$

Now we obtain the explicit expression of $e^{-i\Delta z\hat{V}}$, although it is difficult to calculate exponentials of differential operators in Eq. (4) with the matrix expressions as Eqs. (5) and (6). In Sec. II A. we introduce an additional treatment of the differential operator to acquire simple expressions of the partial evolution operators.

A. Exponentials of differential operators

In Eqs. (5) and (6), discretized expressions of differential operators were given. Here we present an additional treatment called "space splitting" [29] that simplifies the calculation of the exponential functions and gives explicit expressions of the exponentials, i.e., the partial evolution operators. Space-splitting formulations of first-order and second-order differential operators have already been reported earlier in Ref. [30]; nevertheless, we describe them again because they are required in the space-splitting formulation of third-order differential operators.

1. First-order differential operator

Space splitting is a procedure to separate a matrix representation of a differential operator into two block-diagonal matrices. For $\partial/\partial\tau$, even ($\boldsymbol{D}^{(e)}$) and odd ($\boldsymbol{D}^{(o)}$) parts are defined as the following:

$$\left(\frac{\partial}{\partial\tau}\right)_{ab} = \frac{1}{2\Delta\tau}\left[\begin{pmatrix} 0 & 1 & & & \\ -1 & 0 & & & \\ & & 0 & 1 & \\ & & -1 & 0 & \\ & & & & \ddots \end{pmatrix} + \begin{pmatrix} 0 & 0 & & & \\ 0 & 0 & 1 & & \\ & -1 & 0 & & \\ & & & 0 & 0 \\ & & & 0 & 0 \end{pmatrix}\right]$$

$$= \frac{1}{2\Delta\tau}[(\boldsymbol{D}^{(e)})_{ab} + (\boldsymbol{D}^{(o)})_{ab}], \quad (9)$$

where we assume that the total number of the lattice points in the τ direction, N_τ, is an even number.

For notational simplicity, the even and odd parts of the first-order differential operator are expressed as direct sums of 2×2 matrices

$$\boldsymbol{D}^{(e)} = \boldsymbol{d}_0^{(e)} \oplus \boldsymbol{d}_1^{(e)} \oplus \cdots \oplus \boldsymbol{d}_{N_\tau/2-1}^{(e)},$$

$$\boldsymbol{D}^{(o)} = 0 \oplus \boldsymbol{d}_0^{(o)} \oplus \cdots \oplus \boldsymbol{d}_{N_\tau/2-2}^{(o)} \oplus 0. \quad (10)$$

Here,

$$\boldsymbol{d}_n^{(e,o)} = \begin{pmatrix} 0 & 1 \\ -1 & 0 \end{pmatrix}\begin{cases} n = 0,1,\ldots,N_\tau/2-1 & \text{for } \boldsymbol{d}^{(e)} \\ n = 0,1,\ldots,N_\tau/2-2 & \text{for } \boldsymbol{d}^{(o)} \end{cases}, \quad (11)$$

in which $\boldsymbol{d}_n^{(e,o)}$ act only on the temporal subscript a: explicitly written, $\boldsymbol{d}_n^{(e)}$ operates between $\phi_{ik(2n)}$ and $\phi_{ik(2n+1)}$, while $\boldsymbol{d}_n^{(o)}$ operates between $\phi_{ik(2n+1)}$ and $\phi_{ik(2n+2)}$ without intersection among ϕ_{ika}'s with different i or k.

With the help of the direct sum decomposition [Eq. (10)], exponentials of the differential operators can be easily obtained

$$e^{\beta\boldsymbol{D}^{(e)}} = \exp(\beta'\boldsymbol{d}_0^{(e)}) \oplus \exp(\beta'\boldsymbol{d}_1^{(e)}) \oplus \cdots \oplus \exp(\beta'\boldsymbol{d}_{N_\tau/2-1}^{(e)}),$$

$$e^{\beta \boldsymbol{D}^{(o)}} = 1 \oplus \exp(\beta' \boldsymbol{d}_0^{(e)}) \oplus \cdots \oplus \exp(\beta' \boldsymbol{d}_{N_\tau/2-2}^{(e)}) \oplus 1, \tag{12}$$

where β is a real parameter $[\beta' = \beta/(2\Delta\tau)]$ and

$$[\exp(\beta' \boldsymbol{d}^{(e,o)})]_{ab} = \begin{pmatrix} \cos\beta' & \sin\beta' \\ -\sin\beta' & \cos\beta' \end{pmatrix}. \tag{13}$$

It is noted that "1" in the direct-sum decomposition of $\exp(\beta \boldsymbol{D}^{(o)})$ [Eq. (12)] means a simple multiplication of a scalar number 1. Such special features of the spatially split odd differential operators at both edges is universally observed in other odd operators.

Practically, the first-order derivative in Eq. (1), V_τ, has a position-dependent coefficient, i.e., $|\phi_{ika}|^2$. This position-dependent coefficient is represented as a diagonal matrix that acts on the temporal subscript from the left side of $(\partial/\partial\tau)_{ab}$

$$(|\phi|^2)_{ab} = \begin{pmatrix} |\phi_{ik0}|^2 & 0 & \cdots & 0 \\ 0 & |\phi_{ik1}|^2 & \ddots & \vdots \\ \vdots & \ddots & \ddots & 0 \\ 0 & \cdots & 0 & |\phi_{ik(N_\tau/2-1)}|^2 \end{pmatrix}. \tag{14}$$

The operation of Eq. (14) modifies Eq. (12) and gives

$$\exp(\beta|\phi|^2 \boldsymbol{D}^{(e)}) = \exp(\beta' \boldsymbol{d}_0'^{(e)}) \oplus \exp(\beta' \boldsymbol{d}_1'^{(e)}) \oplus \cdots \oplus \exp(\beta' \boldsymbol{d}_{N_\tau/2-1}'^{(e)}),$$

$$\exp(\beta|\phi|^2 \boldsymbol{D}^{(o)}) = 1 \oplus \exp(\beta' \boldsymbol{d}_0'^{(o)}) \oplus \cdots \oplus \exp(\beta' \boldsymbol{d}_{N_\tau/2-2}'^{(o)}) \oplus 1, \tag{15}$$

where

$$\exp(\beta' \boldsymbol{d}_n'^{(e)}) = \begin{pmatrix} \cos\beta'' & \alpha_n^{(e)} \sin\beta'' \\ -(\alpha_n^{(e)})^{-1} \sin\beta'' & \cos\beta'' \end{pmatrix}$$

$$\left(\alpha_n^{(e)} = \frac{|\phi_{ik(2n)}|}{|\phi_{ik(2n+1)}|}, \beta'' = \beta' |\phi_{ik(2n)}||\phi_{ik(2n+1)}| \right) \tag{16}$$

for even parts and

$$\exp(\beta' \boldsymbol{d}_n'^{(o)}) = \begin{pmatrix} \cos\beta'' & \alpha_n^{(o)} \sin\beta'' \\ -(\alpha_n^{(o)})^{-1} \sin\beta'' & \cos\beta'' \end{pmatrix}$$

$$\left(\alpha_n^{(o)} = \frac{|\phi_{ik(2n+1)}|}{|\phi_{ik(2n+2)}|}, \beta'' = \beta' |\phi_{ik(2n+1)}||\phi_{ik(2n+2)}| \right) \tag{17}$$

for odd parts.

2. Second-order differential operator

Here we formulate exponential operators of the second-order differential operator, for example, $\partial^2/\partial x^2$. The space splitting into even $(\boldsymbol{M}_x^{(e)})$ and odd $(\boldsymbol{M}_x^{(o)})$ parts is performed in a similar way to the derivation of Eq. (9) with Eq. (5)

$$\left(-\frac{\partial^2}{\partial x^2} \right)_{ij} = \frac{1}{(\Delta x)^2} \left[\begin{pmatrix} 1 & -1 & & & & \\ & & 0 & & & \\ -1 & 1 & & & & \\ & & & 1 & -1 & \\ 0 & & & & & \\ & & & -1 & 1 & \\ & & & & & \ddots \end{pmatrix} + \begin{pmatrix} 1 & 0 & & & & \\ & 1 & -1 & & & \\ 0 & & & 0 & & \\ & -1 & 1 & & & \\ & 0 & & \ddots & 0 & \\ & & & 0 & 1 & \end{pmatrix} \right]$$

$$= \frac{1}{(\Delta x)^2} [(\boldsymbol{M}_x^{(e)})_{ij} + (\boldsymbol{M}_x^{(o)})_{ij}], \tag{18}$$

where the total number of the lattice points in the x direction, N_x, are again assumed as an even number. Direct-sum decompositions of the even and odd parts become

$$\boldsymbol{M}_x^{(e)} = \boldsymbol{m}_0^{(e)} \oplus \boldsymbol{m}_1^{(e)} \oplus \cdots \oplus \boldsymbol{m}_{N_x/2-1}^{(e)}$$

$$\boldsymbol{M}_x^{(o)} = 1 \oplus \boldsymbol{m}_0^{(o)} \oplus \cdots \oplus \boldsymbol{m}_{N_x/2-2}^{(o)} \oplus 1 \tag{19}$$

with

$$\boldsymbol{m}_n^{(e,o)} = \begin{pmatrix} 1 & -1 \\ -1 & 1 \end{pmatrix} \begin{cases} n = 0,1,\ldots,N_x/2-1 & \text{for } \boldsymbol{m}^{(e)} \\ n = 0,1,\ldots,N_x/2-2 & \text{for } \boldsymbol{m}^{(o)} \end{cases}, \tag{20}$$

where $\boldsymbol{m}_n^{(e,o)}$ act only on the subscript i and produce linear combinations of the two neighboring elements in the x direction. Explicitly, $\boldsymbol{m}_n^{(e)}$ works between $\phi_{(2n)ka}$ and $\phi_{(2n+1)ka}$, whereas $\boldsymbol{m}_n^{(o)}$ works between $\phi_{(2n+1)ka}$ and $\phi_{(2n+2)ka}$, without any action among ϕ_{ika}'s with different k or a.

By using the direct-sum decomposition of Eq. (19), we obtain exponentials of the second-order differential operators

$$e^{\gamma \boldsymbol{M}_x^{(e)}} = \exp(\gamma' \boldsymbol{m}_0^{(e)}) \oplus \exp(\gamma' \boldsymbol{m}_1^{(e)}) \oplus \cdots \oplus \exp(\gamma' \boldsymbol{m}_{N_x/2-1}^{(e)}),$$

$$e^{\gamma' \boldsymbol{M}_x^{(o)}} = e^{\gamma'} \oplus \exp(\gamma' \boldsymbol{m}_0^{(o)}) \oplus \cdots \oplus \exp(\gamma' \boldsymbol{m}_{N_x/2-2}^{(o)}) \oplus e^{\gamma'}, \tag{21}$$

where $\gamma' = \gamma/\Delta x^2$ and

$$[\exp(\gamma' \boldsymbol{m}^{(e,o)})]_{ij} = \frac{1}{2} \begin{pmatrix} 1+e^{2\gamma'} & 1-e^{2\gamma'} \\ 1-e^{2\gamma'} & 1+e^{2\gamma'} \end{pmatrix}. \tag{22}$$

It is noted that the second-order differential operators with respect to other directions (y and τ) are obtained by simply changing the subscript ij in Eq. (22) to kl and ab for y and τ directions, respectively. In the practical calculation, γ is a pure imaginary number, thus the exponential functions are

represented as combinations of sine and cosine functions with a real variable.

3. Third-order differential operator

The remaining of differential operators in MNLSE are the third-order ones that complicate the procedures. However, we can also apply space splitting by treating them as operators with operator-valued coefficients. As an example of third-order differential operators, we consider $(\partial/\partial\tau)\times(-\partial^2/\partial x^2)$ here, but the discussion can also be applied to $(\partial/\partial\tau)(-\partial^2/\partial y^2)$. It is noted that $\partial/\partial\tau$ and $(-\partial^2/\partial x^2)$ are commutative, and that $(\partial/\partial\tau)(-\partial^2/\partial x^2)$ and $(-\partial^2/\partial x^2)(\partial/\partial\tau)$ give the same final results given in the following discussion.

To derive the partial evolution operator defined as an exponential of a third-order differential operator, we first apply space splitting to $(-\partial^2/\partial x^2)$ and $\partial/\partial\tau$. Introducing a parameter δ, the space splitting yields four terms, i.e.,

$$\delta\frac{\partial}{\partial\tau}\left(-\frac{\partial^2}{\partial x^2}\right) = \delta(\boldsymbol{M}_x^{(e)}+\boldsymbol{M}_x^{(o)})(\boldsymbol{D}^{(e)}+\boldsymbol{D}^{(o)}) = \boldsymbol{\varepsilon}^{(e)}\boldsymbol{D}_\tau^{(e)}+\boldsymbol{\varepsilon}^{(o)}\boldsymbol{D}_\tau^{(e)}+\boldsymbol{\varepsilon}^{(e)}\boldsymbol{D}_\tau^{(o)}+\boldsymbol{\varepsilon}^{(o)}\boldsymbol{D}_\tau^{(o)}, \tag{23}$$

where $\boldsymbol{\varepsilon}^{(e,o)}(=\delta\boldsymbol{M}_x^{(e,o)})$ denote the operator-valued coefficients. With this expression, we can obtain the exponential operator by using Eqs. (11), (13), and (14), although we must notice the difference between the coefficients, i.e., $\boldsymbol{\varepsilon}$ and β. At this stage, we calculate exponential functions of $\boldsymbol{D}_\tau^{(e,o)}$ treating $\boldsymbol{\varepsilon}$ as operator-valued coefficients. The results are

$$e^{\boldsymbol{\varepsilon}\boldsymbol{D}^{(e)}} = \exp(\boldsymbol{\varepsilon}'\boldsymbol{d}_0^{(e)})\oplus\exp(\boldsymbol{\varepsilon}'\boldsymbol{d}_1^{(e)})\oplus\cdots\oplus\exp(\boldsymbol{\varepsilon}'\boldsymbol{d}_{N_x/2-1}^{(e)}),$$

$$e^{\boldsymbol{\varepsilon}\boldsymbol{D}^{(o)}} = 1\oplus\exp(\boldsymbol{\varepsilon}'\boldsymbol{d}_0^{(o)})\oplus\cdots\oplus\exp(\boldsymbol{\varepsilon}'\boldsymbol{d}_{N_x/2-2}^{(o)})\oplus 1 \tag{24}$$

with $\boldsymbol{\varepsilon}'=\boldsymbol{\varepsilon}/(2\Delta\tau)=\delta\boldsymbol{M}_x/(2\Delta\tau)$ and

$$[\exp(\boldsymbol{\varepsilon}'_{ij}\boldsymbol{d}^{(e,o)})]_{ab} = \begin{pmatrix} (\cos\boldsymbol{\varepsilon}')_{ij} & (\sin\boldsymbol{\varepsilon}')_{ij} \\ -(\sin\boldsymbol{\varepsilon}')_{ij} & (\cos\boldsymbol{\varepsilon}')_{ij}\end{pmatrix}. \tag{25}$$

For notational simplicity, the subscripts of $\boldsymbol{\varepsilon}$ (i.e., i, j) are dropped during the evaluation from Eq. (23) to Eq. (25), but supplemented in the final results. The superscripts denoting space-splitting components (e,o) are also dropped but the above formulas are correct for both even and odd $\boldsymbol{\varepsilon}$. It is noted that the above matrix representations of "exponential operators with operator-valued elements" act only on the temporal subscript. To stress this fact, we explicitly write down the temporal (a,b) and spatial (i,j) subscripts in Eq. (25).

Each element of the matrix representation in Eq. (25) is a trigonometric function of $\boldsymbol{\varepsilon}^{(e,o)}$. Introducing $\delta'=\delta/(2\Delta\tau\Delta x^2)$, the matrix elements are given in the similar way to Eq. (22), and become

$$\begin{aligned}
\cos(\delta'\boldsymbol{M}_x^{(e)}) &= \boldsymbol{f}_0^{(e)}\oplus\boldsymbol{f}_1^{(e)}\oplus\cdots\oplus\boldsymbol{f}_{N_x/2-1}^{(e)},\\
\cos(\delta'\boldsymbol{M}_x^{(o)}) &= \cos\delta'\oplus\boldsymbol{f}_0^{(o)}\oplus\cdots\oplus\boldsymbol{f}_{N_x/2-2}^{(o)}\oplus\cos\delta',\\
\sin(\delta'\boldsymbol{M}_x^{(e)}) &= \boldsymbol{g}_0^{(e)}\oplus\boldsymbol{g}_1^{(e)}\oplus\cdots\oplus\boldsymbol{g}_{N_x/2-1}^{(e)},\\
\sin(\delta'\boldsymbol{M}_x^{(o)}) &= \sin\delta'\oplus\boldsymbol{g}_0^{(o)}\oplus\cdots\oplus\boldsymbol{g}_{N_x/2-2}^{(o)}\oplus\sin\delta',
\end{aligned} \tag{26}$$

where $\boldsymbol{f}_m^{(e)}$ and $\boldsymbol{g}_m^{(e)}$ are 2×2 matrices that act on the spatial subscripts $(2m,2m+1)$, i.e.,

$$\boldsymbol{f}_m^{(e)} = \begin{array}{c} \\ 2m \\ 2m+1\end{array}\begin{array}{c}\begin{array}{cc} 2m & 2m+1\end{array}\\ \begin{pmatrix} \dfrac{1+\cos(2\delta')}{2} & \dfrac{1-\cos(2\delta')}{2} \\ \dfrac{1-\cos(2\delta')}{2} & \dfrac{1+\cos(2\delta')}{2}\end{pmatrix}\end{array},$$

$$\boldsymbol{g}_m^{(e)} = \begin{array}{c} \\ 2m \\ 2m+1\end{array}\begin{array}{c}\begin{array}{cc} 2m & 2m+1\end{array}\\ \begin{pmatrix} \dfrac{\sin(2\delta')}{2} & -\dfrac{\sin(2\delta')}{2} \\ -\dfrac{\sin(2\delta')}{2} & \dfrac{\sin(2\delta')}{2}\end{pmatrix}\end{array}. \tag{27}$$

Here, $\boldsymbol{f}_m^{(o)}$ and $\boldsymbol{g}_m^{(o)}$ have the same expressions as $\boldsymbol{f}_m^{(e)}$ and $\boldsymbol{g}_m^{(e)}$, respectively, but they act only on the spatial subscript of $(2m+1,2m+2)$. As a result, the matrix representation of the evolution operator becomes a matrix (with temporal subscripts) whose elements are again matrices (with spatial subscripts).

Now exponentials of the third-order differential operators are obtained; however, it is difficult to intuitively understand the action of the exponential operators from the above formulas. To demonstrate the operation of Eq. (27), we demonstrate the matrix action of Eq. (26) on the envelope ϕ_{ika} as a linear relationship. For example, the action of $\exp[\delta\boldsymbol{D}^{(e)}\boldsymbol{M}_x^{(e)}]$ is obtained by applying Eq. (25) on ϕ with care for treatment of the subscripts. The first step is an operation on the temporal subscript, i.e.,

$$\begin{pmatrix}\phi'_{ik(2n)}\\ \phi'_{ik(2n+1)}\end{pmatrix} = \begin{pmatrix}[\cos(\delta'\boldsymbol{M}_x^{(e)})]_{ij} & [\sin(\delta'\boldsymbol{M}_x^{(e)})]_{ij}\\ -[\sin(\delta'\boldsymbol{M}_x^{(e)})]_{ij} & [\cos(\delta'\boldsymbol{M}_x^{(e)})]_{ij}\end{pmatrix}\begin{pmatrix}\phi_{jk(2n)}\\ \phi_{jk(2n+1)}\end{pmatrix}. \tag{28}$$

In the above expression, a summation with respect to the repeated subscript j should be taken, and ϕ' denotes the value after evolution, i.e., $\phi'=\exp[\delta\boldsymbol{D}^{(e)}\boldsymbol{M}_x^{(e)}]\phi$.

It is noted that matrix elements on the rhs of Eq. (28) are still matrices. Substituting Eqs. (26) and (27) into Eq. (28), we obtain the final result, where all elements are scalar values

$$\begin{pmatrix} \phi'_{(2m)k(2n)} \\ \phi'_{(2m+1)k(2n)} \\ \phi'_{(2m)k(2n+1)} \\ \phi'_{(2m+1)k(2n+1)} \end{pmatrix} = \begin{pmatrix} \frac{1+\cos 2\delta'}{2} & \frac{1-\cos 2\delta'}{2} & \frac{\sin 2\delta'}{2} & -\frac{\sin 2\delta'}{2} \\ \frac{1-\cos 2\delta'}{2} & \frac{1+\cos 2\delta'}{2} & -\frac{\sin 2\delta'}{2} & \frac{\sin 2\delta'}{2} \\ -\frac{\sin 2\delta'}{2} & \frac{\sin 2\delta'}{2} & \frac{1+\cos 2\delta'}{2} & \frac{1-\cos 2\delta'}{2} \\ \frac{\sin 2\delta'}{2} & -\frac{\sin 2\delta'}{2} & \frac{1-\cos 2\delta'}{2} & \frac{1+\cos 2\delta'}{2} \end{pmatrix} \begin{pmatrix} \phi_{(2m)k(2n)} \\ \phi_{(2m+1)k(2n)} \\ \phi_{(2m)k(2n+1)} \\ \phi_{(2m+1)k(2n+1)} \end{pmatrix}. \tag{29}$$

The total operation of $\exp[\delta \boldsymbol{D}^{(e)} \boldsymbol{M}_x^{(e)}]$ is given as a direct sum of Eq. (29). Explicit expressions of other terms in Eq. (23), i.e., $\exp(\delta \boldsymbol{D}^{(e)} \boldsymbol{M}_x^{(o)})$, $\exp(\delta \boldsymbol{D}^{(o)} \boldsymbol{M}_x^{(e)})$, and $\exp(\delta \boldsymbol{D}^{(o)} \boldsymbol{M}_x^{(o)})$, are obtained similarly with care for edge parts of the odd operators.

B. Exponential product expansion of evolution operator

The total Hamiltonian is decomposed into 17 terms due to the space-splitting treatment in Sec. II A, i.e.,

$$\begin{aligned} \hat{H} = {} & \hat{K}_{\tau\tau}^{(e)} + \hat{K}_{xx}^{(e)} + \hat{K}_{yy}^{(e)} + \hat{K}_{\tau\tau}^{(o)} + \hat{K}_{xx}^{(o)} + \hat{K}_{yy}^{(o)} + \hat{V} + \hat{V}_{\tau}^{(e)} + \hat{V}_{\tau}^{(o)} \\ & + \hat{K}_{\tau xx}^{(ee)} + \hat{K}_{\tau xx}^{(eo)} + \hat{K}_{\tau xx}^{(oe)} + \hat{K}_{\tau xx}^{(oo)} + \hat{K}_{\tau yy}^{(ee)} + \hat{K}_{\tau yy}^{(eo)} + \hat{K}_{\tau yy}^{(oe)} \\ & + \hat{K}_{\tau yy}^{(oo)}. \end{aligned} \tag{30}$$

Here, the superscripts e and o denote even and odd components of spatially split differential operators, respectively. For the third-order differential operators, two superscripts indicate the spatially split components of the differential operators with respect to the temporal and spatial directions, e.g., $\hat{K}_{\tau xx}^{(eo)}$ means $\exp(\delta \boldsymbol{D}^{(o)} \boldsymbol{M}_x^{(e)})$ in Eq. (23). Applying the second-order symmetrical decomposition formula given in Eq. (3), we obtain the following EPE:

$$S_2(\Delta z) = \hat{U}_{\mathrm{o}}^{*}(\Delta z) \hat{U}_{\mathrm{e}}^{*}(\Delta z) \hat{U}_V(\Delta z) \hat{U}_{\mathrm{e}}(\Delta z) \hat{U}_{\mathrm{o}}(\Delta z), \tag{31}$$

where S_2 denotes the second-order symmetric decomposition of the evolution operator. In Eq. (31), the partial evolution operators are categorized as

$$\hat{U}_V(\Delta z) = e^{-i\Delta z \hat{V}_{\tau}^{(o)}/2} e^{-i\Delta z \hat{V}_{\tau}^{(e)}/2} e^{-i\Delta z \hat{V}} e^{-i\Delta z \hat{V}_{\tau}^{(e)}/2} e^{-i\Delta z \hat{V}_{\tau}^{(o)}/2},$$

$$\begin{aligned} \hat{U}_{\mathrm{e}}(\Delta z) = {} & e^{-i\Delta z \hat{K}_{\tau xx}^{(eo)}/2} e^{-i\Delta z \hat{K}_{xx}^{(o)}/2} e^{-i\Delta z \hat{K}_{\tau xx}^{(oo)}/2} \\ & \times e^{-i\Delta z \hat{K}_{\tau\tau}^{(o)}/2} e^{-i\Delta z \hat{K}_{\tau xx}^{(oe)}/2} e^{-i\Delta z \hat{K}_{\tau yy}^{(oe)}/2} \\ & \times e^{-i\Delta z \hat{K}_{\tau xx}^{(ee)}/2} e^{-i\Delta z \hat{K}_{\tau yy}^{(ee)}/2} e^{-i\Delta z \hat{K}_{\tau\tau}^{(e)}/2} \\ & \times e^{-i\Delta z \hat{K}_{xx}^{(e)}/2} e^{-i\Delta z \hat{K}_{yy}^{(e)}/2}, \end{aligned}$$

$$\hat{U}_{\mathrm{o}}(\Delta z) = e^{-i\Delta z \hat{K}_{\tau yy}^{(oo)}/2} e^{-i\Delta z \hat{K}_{\tau yy}^{(eo)}/2} e^{-i\Delta z \hat{K}_{yy}^{(o)}/2}. \tag{32}$$

In Eq. (31), $*$ denotes reverting the order of the operators defined in Eq. (32). There is arbitrariness in the order, so different alignments are also possible. In the above expression, the operator ordering is determined so that the computational cost and time are minimized as much as possible. For example, $e^{-i\Delta z \hat{V}}$ is placed at the center of S_2 to avoid repeated evaluation, because it requires the longest computation time among all exponential operators. On the other hand, exponentials of differential operators are finally reduced to simple multiplications of constant coefficients [Eq. (29)] and they produce little load in the calculation, even if evaluated repeatedly.

In the practical calculations, we use the second-order formula, but a higher-order decomposition formula is also available as a product of the second-order formulas;

$$F^{(n)}(\Delta z) = \prod_{i=1}^{N_n} S_2(p_i^{(n)} \Delta z). \tag{33}$$

For example, a fourth-order decomposition is given with $N_4 = 5$ and the following $\{p_i^{(4)}\}_{i=1,\cdots,5}$'s [24,25]:

$$p_1^{(4)} = p_2^{(4)} = p_4^{(4)} = p_5^{(4)} = 0.414\,490\,771\,794\,376,$$

$$p_3^{(4)} = -0.657\,963\,087\,177\,503\,0. \tag{34}$$

Using the EPE procedure, we can calculate "long-time" evolution by repeating "short-time" evolution. It should be stressed that the numerical error is restricted to an extent during the long-time evolution due to the feature of EPE [23–28].

It is noted that the number of required calculation steps in the present method is proportional to a total data number N. This leads to the calculation steps required for the higher-order formula becoming simply N_n times of that for the second-order formula. The higher-order calculation according to Eq. (33) is also possible with SSF method, though it requires additional calculation steps due to the repeated usage of fast Fourier transformation that consists of $\sim O(N \log_{10} N)$ calculation steps. Therefore, the present method has an advantage in calculating larger systems with higher precision.

There is another merit in the formulation using space splitting. The space-splitting procedure reduces the matrix expression of the evolution operator to a product of block-diagonal matrices as shown in the previous sections. Here, each block-diagonal matrix affects only a pair of the ele-

ments of $\{\phi_{ika}\}$ that align side by side, leaving other elements unchanged. This means that the evolution operation consists of local operations which can be independently performed, that is, the present method is a subject of parallel computation. In this work, calculations are performed using a workstation equipped with two Pentium-4 CPUs (2.8 GHz clock on 400 MHz processor bus) in parallel on the two CPUs; however, the program itself is designed to work on more than three CPUs. The calculation time for 1400 evolution steps of $384\times384\times384$ data is about 11 h and is proportional to the number of data and evolution steps. By suitably aligning the array of $\phi_0(x,y,\tau)$, we can efficiently perform the parallel computing on larger computer systems, such as cluster computing systems.

C. Plasma defocusing effects

To take into account the effects of plasma defocusing in nitrogen gas, the following terms must be added to the rhs of Eq. (1) to modify the MNLSE to ENLSE [1,6]:

$$-\frac{ik_0}{2}\left(1-\frac{i}{\omega_0}\frac{\partial}{\partial\tau}\right)\left(\frac{\rho}{\rho_c}\phi\right)-\frac{11}{2}(\rho_0-\rho)\sigma_{11}\hbar\omega_0(|\phi|^2)^{10}\phi, \tag{35}$$

where ρ denotes a plasma density that is produced through the 11-photon ionization process of the nitrogen molecule with $\lambda=800$ nm light; ρ is determined with the following equation according to a Drude model:

$$\frac{\partial\rho}{\partial\tau}=\sigma_{11}(|\phi|^2)^{11}(\rho_0-\rho). \tag{36}$$

In the above equations, ρ_0 and ρ_c are the initial density of nitrogen molecule and critical plasma density, respectively, and σ_{11} is the cross section of 11-photon absorption of the nitrogen molecule.

The plasma effects can be accounted into the present method by replacing interaction terms V and V_τ in Eq. (4) with the following alternative ones, respectively,

$$\hat{V}'=-n_2k_0\left(|\phi|^2-\frac{1}{2n_2\rho_c}\rho\right)-i\frac{n_2k_0}{\omega_0}\left(\frac{\partial|\phi|^2}{\partial\tau}+\frac{1}{2n_2\rho_c}\frac{\partial\rho}{\partial\tau}\right)-i\frac{11}{2}(\rho_0-\rho)\sigma_{11}\hbar\omega_0(|\phi|^2)^{10}, \tag{37}$$

$$\hat{V}'_\tau=-i\frac{n_2k_0}{\omega_0}\left(|\phi|^2+\frac{1}{2n_2\rho_c}\rho\right)\frac{\partial}{\partial\tau}. \tag{38}$$

In the present method, ρ must be evaluated five times per z-evolution step. This is because ρ is determined for a given ϕ at each time when calculating the z evolution due to interaction terms and because the interaction part of the evolution operator, $\hat{U}_V(\Delta z)$ in Eq. (32), consists of five partial evolution operators. In the practical calculation, $\rho(\tau)$ is obtained by applying Simpson's formula to the analytical solution of Eq. (36), i.e.,

TABLE I. Parameters used in the calculation. All values are reduced for $\lambda=800$ nm light in nitrogen gas. The Kerr nonlinear refractive index (n_2) and density of nitrogen molecules (ρ_0) are proportional to the gas pressure (p); ρ_0 is dependent on the gas temperature and chosen as that at 300 K.

Parameters	Units	Values in N_2 at p (atm)
V_g	m/s	3.00×10^8
β_2	s^2/m	2.13×10^{-29}
k_0	/m	7.85×10^6
n_0		1.00
n_2[a]	m^2/W	$3.20p\times10^{-23}$
ρ_0[a]	$/m^3$	$2.44p\times10^{25}$
ρ_c[a]	$/m^3$	1.74×10^{27}
σ_{11}[a]	$m^{22}/(sW^{11})$	5.08×10^{-188}

[a]Reference [6].

$$\rho(\tau)=\rho_0-\rho_0\exp\left\{-\sigma_{11}\int_0^\tau d\tau'[|\phi(\tau')|^2]^{11}\right\}, \tag{39}$$

to save calculation time.

Table I lists the material parameters used in the calculation to clarify the calculation conditions. These parameters are determined in reference to Ref. [6] with modifications for matching with the experimental condition in Ref. [10], e.g., the parameters are converted to those for the light whose wavelength is $\lambda=800$ nm. As the gas medium is dilute, the refractive index n_0, group velocity of light V_g, and wave number k_0 are chosen as those in a vacuum. The Kerr refraction index n_2 is proportional to the gas pressure p (atm) through dependency on the gas density. The density of nitrogen molecules ρ_0 depends on the gas temperature as well as on the gas pressure. In Table I, we show a reduced value of ρ_0 to that at 300 K using the Boyle-Charles law. The group velocity dispersion β_2 can also depend on p, though the change of β_2 with respect to p is too small to observe. Consequently, the pressure dependence is considered only for ρ_0 and n_2 in this paper.

Parameters concerning plasma formation are chosen as follows: $\rho_c\equiv m\epsilon_0\omega_0^2/e^2$ is a critical plasma density, where e and m are electron charge and mass, respectively, ω_0 is an angular frequency of the incident light, and ϵ_0 is a permittivity in vacuum. At the light wavelength of $\lambda=800$ nm, the order of multiphoton ionization K_N is 11 with the ionization potential $U_N=15.6$ eV in nitrogen gas. Following the Appendix of Ref. [6], the ionization rate for $\lambda=800$ nm light in nitrogen is calculated according to the Keldysh's theory in the multiphoton ionization limit.

III. RESULTS AND DISCUSSIONS

In this section, we show the calculation results with the method developed in Sec. II. As mentioned earlier, ENLSE describes the pulse propagation observed in the co-moving frame and the evolution integration is performed toward the z direction. As a result, we obtain a set of (2+1)D spatiotemporal data at different z positions. On the other hand, FTOP

is a method for observing temporal snapshot images of propagating light pulses [8–11]. Therefore, to simulate the experimental result of FTOP with calculations, we must convert the calculation result to a set of three-dimensional (3D) spatial data at different times. In this section, all images are converted to temporal snapshots by realigning the (2+1)D spatiotemporal data according to the relation $\tau=t-z/V_g$.

In the typical calculation, the second-order formula is applied to the initial ϕ defined on $384\times384\times384$ points, and the number of evolution steps in the z direction needed to obtain temporal snapshots up to $t=3.2$ ps period is 1400. The spatial resolution is set to $\Delta x=\Delta y=1$ μm in the xy plane. To adjust the z-directional sizes of the converted images to those in the xy plane, the temporal step is chosen as $\Delta\tau=3.34$ fs from $\Delta\tau=\Delta x/V_g$. Thus the initial pulse is defined on the 384×384 μm^2 area in the xy plane and on the 1.28 ps interval in the τ direction, which means that the resultant temporal snapshots are given on the $384\times384\times384$ μm^3 cubic region. Here, the initial pulse is assumed as a Gaussian both in the spatial and temporal directions, with spatial full width at half maximum (FWHM) of 42 μm and temporal FWHM of 144 fs. In the experiment, the incident light pulse is weakly focused with a lens of focal length $f=350$ mm [10]. We approximate the incident light as a collimated beam, that is, the initial pulse has the same spatial FWHM at every time slice, based on the consideration that the spatial FWHM is almost constant in the observed z-directional region.

Here we mention the treatment of the boundary. In this work, numerical calculation is performed on the finite system assuming the Dirichlet's boundary condition, while there are no boundaries in the real system. To suppress the boundary effects, a damping potential of imaginary value is added to the area around 30 μm from the boundaries. The strength of the damping potential varies smoothly as $\cos^2$ according to the distance from the edges to avoid the reflection due to abrupt changes of the potential. In fact, the boundary effect is not observed so far as the light pulses are confined around the center of the observing window [31].

A. Numerical stability and accuracy

The EPE method itself is an unconditionally stable and accurate one for numerical integration, but it fails when the evolution step becomes too large. To obtain the criterion for successful calculation, it is necessary to compare the numerical result with the analytical one. However, this is impossible because no analytical solution of ENLSE is available. According to the study on the one-dimensional free motion in Ref. [27], the second-order De Raedt method [30] becomes unstable in the case of $\Delta t/\Delta x^2>0.5$, where $\Delta t/\Delta x^2$ is a dimensionless time step for the free motion in the x direction. Here we comment on the stability and accuracy of the calculation.

As the present method is an extension of De Raedt's method, we adopt the above discussion to the evolution according to ENLSE beyond SVEA. In the present work, effects of the evolution step may be different from those in Ref. [27]; however, it should be reasonable to estimate the evolution step as a benchmark for stability, because the accuracy of EPE is determined with a power of the evolution step. From Eq. (4), it is noted that a total evolution operator comprises five types of partial evolution operator, i.e., the group velocity dispersion term ($\hat{K}_{\tau\tau}$), the diffraction term ($\hat{K}_{xx},\hat{K}_{yy}$), the shock term in the diffraction ($\hat{K}_{\tau xx},\hat{K}_{\tau yy}$), the Kerr nonlinear term ($\hat{V}$), and the shock term of the Kerr effect ($\hat{V}_\tau$). The partial evolution operators are further split into even and odd parts except the Kerr term, but the evolution step is common for the even and odd parts.

TABLE II. Dimensionless evolution steps for five types of partial evolution operators in Eq. (4). Absolute values are shown for Δ_V and Δ_{V_τ}, because they are complex numbers in definitions. To estimate the upper limit of the stability, values are calculated for the $P_0=0.78$ mJ pulse in nitrogen gas at 4 atm, that give the maximum values of $|\Delta_V|$ and $|\Delta_{V_\tau}|$. As the definition of $|\Delta_V|$, the rhs of Eq. (37) should be referred, for it is too complicated to be shown in the table.

Evolution steps	Definition	Values
$\Delta_{\tau\tau}$	$\Delta z\beta_2/\Delta\tau^2$	1.91×10^{-6}
$\Delta_{xx}=\Delta_{yy}$	$-\Delta z/(k_0n_0\Delta x^2)$	-1.27×10^{-1}
$\Delta_{\tau xx}=\Delta_{\tau yy}$	$\Delta_{xx}/(\omega_0\Delta\tau)$	-8.10×10^{-3}
Δ_V	$\Delta z\times$ [rhs of Eq. (37)]	$\leqslant3.08\times10^{-1}$
Δ_{V_τ}	$-i\Delta z[n_2\lvert\phi\rvert^2+\rho/(2\rho_c)]/V_g$	$\leqslant1.43\times10^{-1}$

Dimensionless evolution steps for the five partial evolution operators are obtained by properly scaling the multiples of the evolution step ($\Delta z=1$ μm) and coefficients of the corresponding differential operators. It is noted that the Kerr nonlinear term is a complex scalar number (not a differential operator) and that the number itself gives the dimensionless evolution step. The results are given in Table II with explicit definitions of the dimensionless evolution steps. The dimensionless evolution steps are expressed as Δ with subscripts denoting the corresponding differential operators; e.g., $\Delta_{\tau\tau}$ is that for the $\partial^2/\partial\tau^2$.

In Table II, the maximum value of $|\phi|^2$ ($=2.55\times10^{18}$ W/m^2 for a $P_0=0.78$ mJ pulse) is applied to estimate the upper limits of $|\Delta_V|$ and $|\Delta_{V_\tau}|$. Similarly, $\partial|\phi|^2/\partial\tau$ is estimated as $|\phi|^2/\Delta\tau$, which gives the maximum value of $\partial|\phi|^2/\partial\tau$. Evolution steps due to the plasma effects can be also estimated with Eqs. (36)–(38) noting $0<\rho/\rho_c\leqslant\rho_0/\rho_c=5.61\times10^{-2}$.

Among all terms, the evolution step due to the plasma defocusing effect is the largest but at most 0.31, satisfying the stability condition of the second-order De Raedt method. Moreover, the maximum value of the evolution steps appears only in the calculation of $P_0=0.78$ mJ light pulses, because the temporal range of the calculation is not long enough to realize the maximum plasma density for weak light pulses. Accordingly, we can predict the stability and accuracy of the second-order calculations, although the discussion given above is not a strict one. Practically, we confirm the stability and accuracy by comparing the results of second-order and fourth-order calculations. Calculation results with half-evolution steps ($\Delta z=0.5$ μm) also support the validity of the second-order calculation.

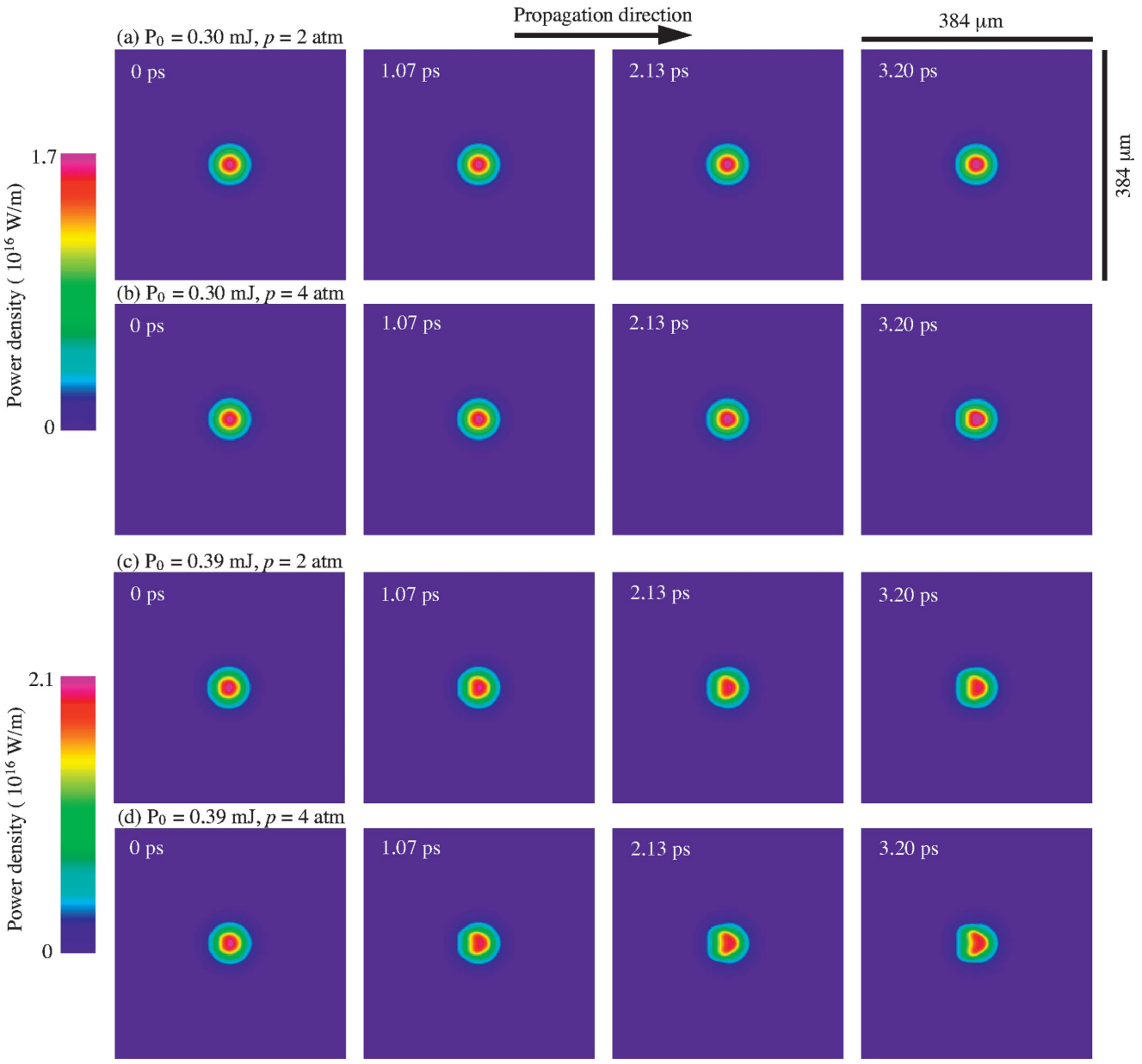

FIG. 1. (Color) Projected spatial intensity distributions of initially Gaussian femtosecond light pulses propagating in nitrogen gas. The vertical and horizontal size is 384×384 μm^2 commonly for all the images. (a) Propagation of initially 0.30 mJ pulse in N_2 of 2 atm. (b) Propagation of initially 0.30 mJ pulse in N_2 of 4 atm. (c) Propagation of initially 0.39 mJ pulse in N_2 of 2 atm. (d) Propagation of initially 0.39 mJ pulse in N_2 of 4 atm. Values of the light intensity are indicated with color palettes on the left of the images that are common for (a, b) and (c, d), respectively. The two-dimensional images are obtained by integrating 3D intensity distribution according to the direction perpendicular to the image planes. The time indicated in each image is the elapsed time from the moment when the initial pulses fully penetrate into the $z>0$ region.

B. Femtosecond pulse propagation in nitrogen gas

Figure 1 shows temporal snapshot images obtained from calculations. The images in Fig. 1 are projections of 3D profiles onto the image plane: that is, $I(x,z;t)=\int dy|\phi(x,y,z;t)|^2$ when the image plane is chosen as the xz plane. This results in the unit of an intensity distribution becoming W/m in the projection images, whereas $|\phi(x,y,z;t)|^2$ gives an intensity distribution in the unit of W/m^2. Moreover, each image is the one observed in the comoving frame: in practice, the light pulses are moving at the group velocity V_g, but such uniform motion is omitted in the figures.

Figure 1 visually shows how the propagation phenomena of light pulses change according to the incident pulse energy (P_0=0.30 and 0.39 mJ) and nitrogen gas pressure (p=2 and 4 atm). Spatial intensity distributions of the pulses are shown in color to highlight the evolutions of pulse forms. The color palettes showing the intensity distributions are common for the images with the same P_0: i.e., images in Figs. 1(a) and 1(b) are scaled by the upper color palette while those in Figs.

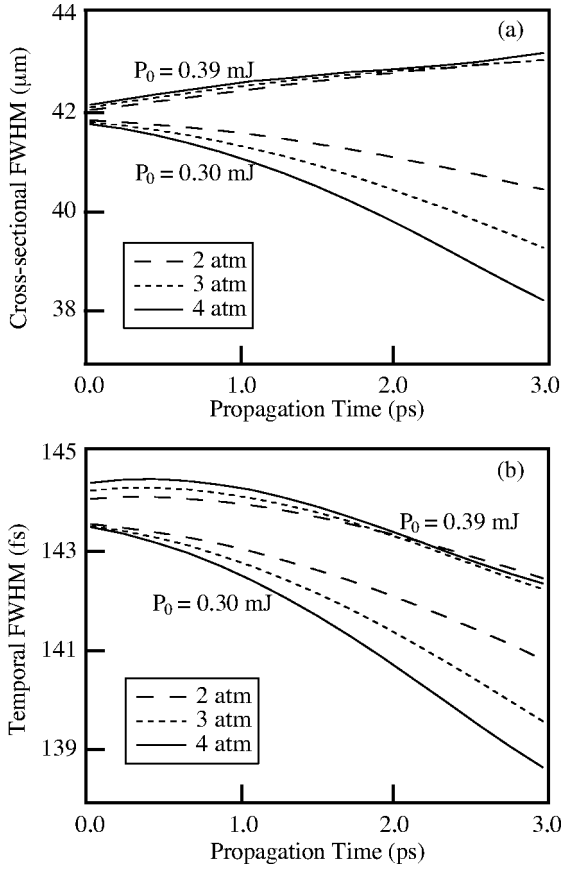

FIG. 2. Temporal evolutions of light pulses during the propagation in the nitrogen gas with different pressures. (a) Evolutions of cross-sectional FWHM in the gas pressures of 2 atm (dashed lines), 3 atm (dotted lines), and 4 atm (solid lines). (b) Evolutions of temporal FWHM in the gas pressures of 2 atm (dashed lines), 3 atm (dotted lines), and 4 atm (solid lines). Results of two different light intensities (0.30 mJ and 0.39 mJ) are also shown in (a) and (b).

1(c) and 1(d) are scaled by the lower one. The light pulse shrinks slightly both in the *xy* and *z* directions throughout the propagation when the light intensity is weak (P_0=0.30 mJ). Contrarily, the light pulses diverge in the *xy* direction when the input pulse energy becomes larger (P_0=0.39 mJ).

To allow detailed study of the propagation phenomena, FWHMs of pulse profiles in the *xy* and *z* directions are calculated by fitting the projections of pulse forms with a suitable function. We show the fitting results in Fig. 2, assuming the Gaussian profile in both the *xy* and *z* directions. This assumption is adopted correspondingly to the analysis in the experiments, although the assumption is not suitable for the calculation results in practice. Here, "Temporal FWHM" in Fig. 2(b) means a FWHM in the *z* direction converted to the temporal width as $\delta z = V_g \delta t$.

The behavior of the P_0=0.30 mJ pulse is phenomenologically similar to the simple self-focusing effect predicted by the NLSE, except that the self-steepening effect due to the shock correction is observed slightly in Fig. 1. The light pulse shrinks as the gas pressure increases, i.e., as the Kerr coefficient n_2 becomes larger. This means that a weak light pulse below 0.30 mJ suffers dominantly from the Kerr self-focusing effect rather than from the plasma defocusing effect. In fact, calculations without plasma defocusing effects show similar results to those for the weak pulse in Figs. 2(a) and 2(b).

On the other hand, the P_0=0.39 mJ pulse shows somewhat complicated propagation behavior. This significant observation is a relative behavior of the pulses in different gas pressures. As seen in Fig. 2(a), the pulse grows in the *xy* direction as the propagation time progresses. The growth increases with the gas pressure, which is the opposite of what is observed for P_0=0.30 mJ pulses. Although the total growth of the pulses in the *xy* direction does not match the experimental results (Fig. 7(c) in Ref. [10]), Fig. 2(a) reproduces the relative change of the pulse propagation under different gas pressures. The results indicate the competition between those two effects working in opposition to each other and that the plasma defocusing effect overcomes the Kerr self-focusing effect for an intense light pulse above P_0 =0.39 mJ. Here, the plasma defocusing effect has significant dependence on the light power compared to the Kerr self-focusing effect, and it changes significantly according to the incident light power. In fact, the nonlinear Kerr self-focusing effect depends on $|\phi|^2$, whereas the plasma defocusing effect involves $(|\phi|^2)^{11}$ for the 11-photon ionization process as seen in Eqs. (36) and (37).

It is difficult to give an intuitive explanation of the propagation behavior of the P_0=0.39 mJ pulse in the *z* direction [Fig. 2(b)]. In addition to the competition between the Kerr self-focusing and plasma-defocusing effects, the self-steepening effect possibly makes the propagation phenomena complicated. In comparison with the experiment [10], the calculation does not reproduce the experimental result quantitatively. Nevertheless, we notice the agreement of Fig. 2(b) with the experimental result (Fig. 7(d) in Ref. [10]): the temporal FWHMs of the light pulses, which are initially $(\delta t)_{p=2} < (\delta t)_{p=3} < (\delta t)_{p=4}$, change their order as $(\delta t)_{p=3} < (\delta t)_{p=4} < (\delta t)_{p=2}$ during the propagation, where $(\delta t)_p$ denotes the temporal FWHM (fs) at the nitrogen pressure *p* (atm).

From the above discussion, we conclude that the present calculation can predict the pulse propagation phenomena in nitrogen gas to some extent, although further consideration is needed for quantitative prediction [32]. We believe progress in theoretical and experimental approaches will improve the correspondence between them.

C. Multiple-cone formation in nitrogen gas

Since the present calculation method includes the shock-term correction, we can apply that method to phenomena where the light intensity varies rapidly in the space time. As an example of such phenomena, we report here the possibility of multiple-cone formation in nitrogen gas.

The multiple-cone structure appears in the high-power regime of the light. In this regime, the dominant plasma effects cause the lights to be defocused, and each fragment that is sufficiently intense to cause the Kerr self-focusing effects but sufficiently weak to avoid the plasma defocusing effect goes into Kerr self-focusing. Consequently, a multiple-cone structure appears, that is also reported in quartz glasses [21,22]. In

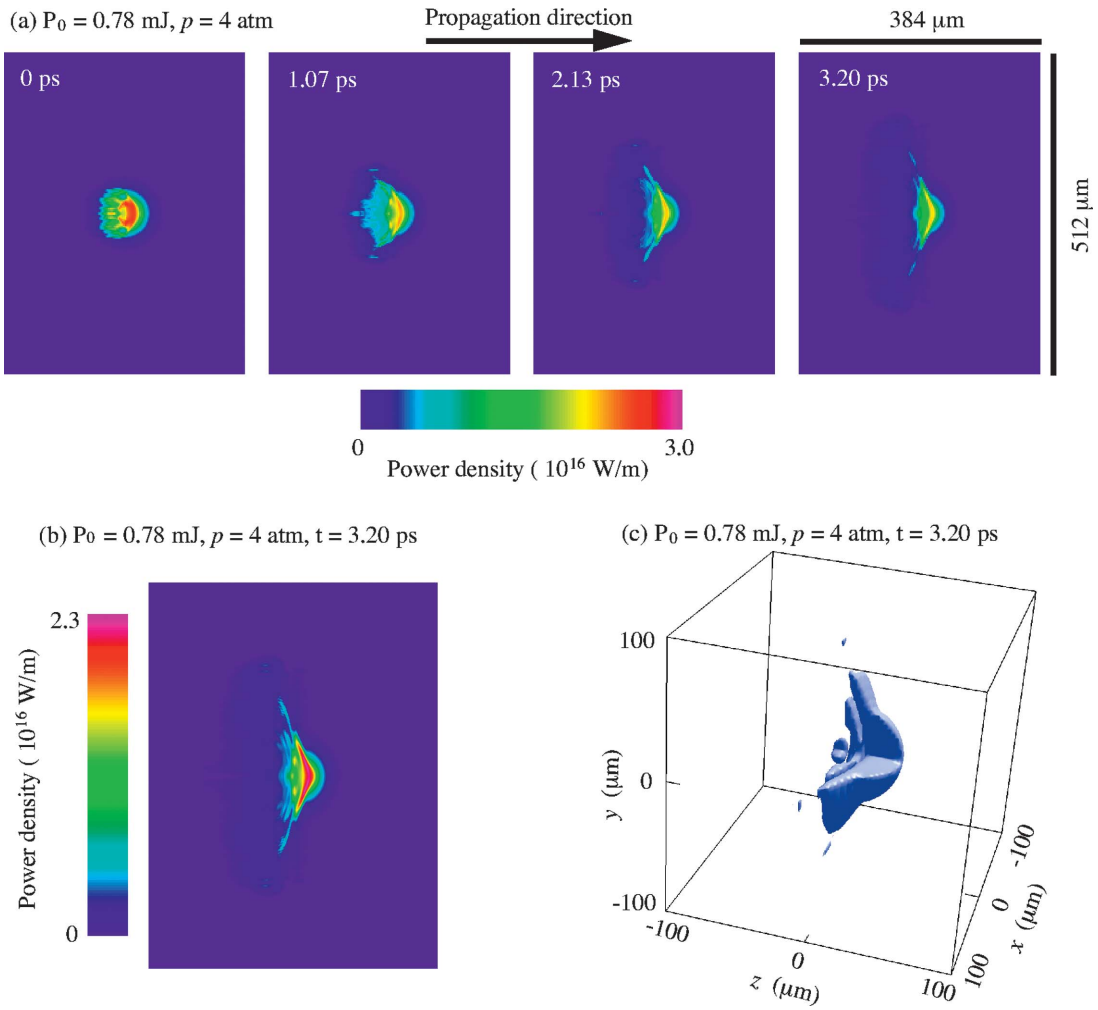

FIG. 3. (Color) Projected spatial intensity distributions of the initially Gaussian light pulses whose energies are P_0=0.78 mJ. The pressure of the N_2 gas is p=4 atm, and other conditions are the same as those in Fig. 1. (a) Projected intensity distributions of the light pulse up to 3.20 ps, (b) same as the snapshot at t=3.20 ps in (a) but the size and color scale are expanded, and, (c) 3D isosurface ($|\phi|^2$=1.89 $\times 10^{17}$ W/m^2) plot of the pulse shape corresponding to (b).

order to realize the multiple-cone formation in nitrogen gas, the input light power is set as twice of what it was in Sec. III B.

Figure 3 shows calculated projection images of a collimated P_0=0.78 mJ light pulse propagating in the p=4 atm nitrogen gas. Generally, the multiple-cone structure appears over a wide area in the space, so the size of the system is extended to 512×512 μm^2 in the xy plane while the range in the z direction remains at 384 μm. The formation process of the multiple-cone structure is shown in Fig. 3(a). The incident light pulse starts to spread due to the plasma defocusing effect (t=1.07 ps) and the spread fragments gather (t=2.13 ps) to finally form the cone structure (t=3.20 ps).

We can also observe that the peak intensity of the light pulses is decreased according to the propagation, for the plasma defocusing effect works to disperse pulses against the Kerr self-focusing effect. Consequently, no clear cone structure appears in the final result of Fig. 3(a). To highlight the fine structure of the multiple cone, a modified image of the t=3.20 ps result in Fig. 3(a), which is expanded both in size and intensity, is shown in Fig. 3(b). We can clearly observe the fourfold cone structure in Fig. 3(b) that is hardly seen in Fig. 3(a).

Considering the cylindrical symmetry of the system, we can draw conclusions about the multiple-cone formation from the projection images. However, the 3D observation does provide direct images of the cone structure. The 3D isosurface plot is shown in Fig. 3(c), which corresponds to Fig. 3(b). Here, the isosurface indicates a set of points where the intensity is equal to 1.89×10^{17} W/m^2, corresponding to 15% of the maximum intensity. Furthermore, a quarter of the pulse is removed for observing a cone structure at the inner part of the pulse. Because of the poor resolution of the isosurface plot, the fourfold cone structure is not shown, but we can distinguish the outermost cone from inner cones as indicated in Fig. 3(b).

The multiple-cone structure of an intense light pulse in the nitrogen gas has not yet been observed in practice due to experimental limitations. We expect our calculations to help reveal the propagation phenomena of high-power laser pulses in gas media.

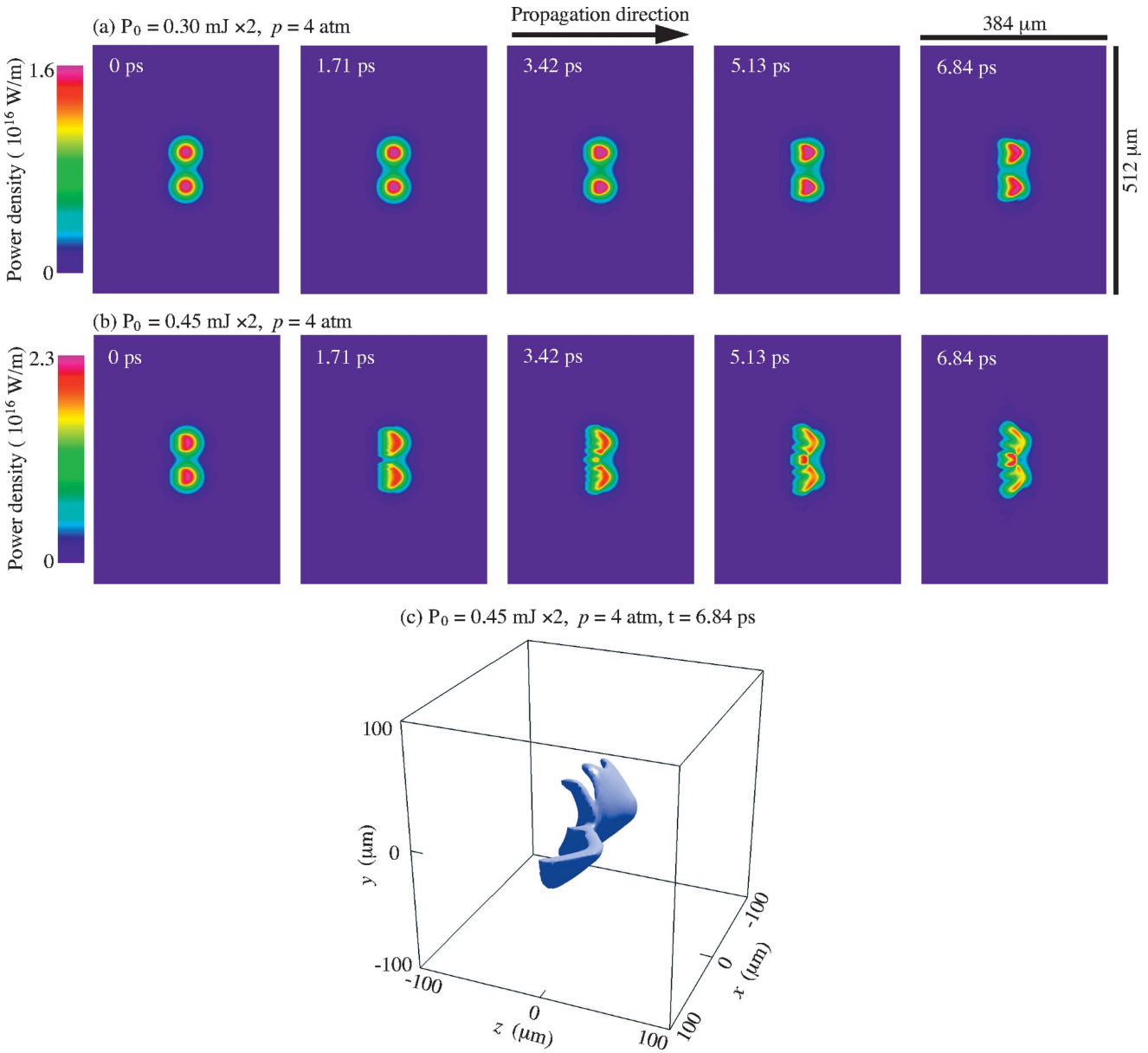

FIG. 4. (Color) Projected spatial intensity distributions of propagating two light pulses that are initially separated with a distance of 35 μm. (a) Projected intensity distributions of two P_0=0.30 mJ light pulses up to 6.84 ps, (b) projected intensity distributions of two P_0 =0.45 mJ light pulses up to 6.84 ps, and (c) 3D isosurface ($|\phi|^2$=6.81×10^{17} W/m^2) plot of the pulse shape corresponding to the t=6.84 ps image of (b). The pressure of the N_2 gas is p=4 atm, while other conditions are the same as those in Fig. 1.

D. Interaction of two femtosecond pulses

One of the key features of the present calculation method is that the method is applicable to the 3D spatially nonsymmetrical phenomena without cylindrical symmetry. As a simple example of the nonsymmetrical phenomena, we demonstrate the interaction between two collimated light pulses. The present method is also effective for calculating pulse propagation in nonsymmetrical environments such as photonic crystal fibers.

Figure 4 shows the propagation of the two collimated light pulses. The distance between two pulses is chosen as 35 μm and the other parameters of the incident light pulse are kept to the same as those in Sec. III B and III C. The nitrogen gas pressure is set to 4 atm to emphasize the nonlinear effects. The area of the snapshot image is chosen as 512×512 μm^3 in the xy direction while the range in the z direction is 384 μm. Note that the evolution is calculated up to 6.84 ps because it takes longer to observe the significant deformation of the light pulses.

Projected snapshot images are shown in Figs. 4(a) and 4(b) to compare the propagation of light pulses with different intensity. Weak pulses (P_0=0.30 mJ×2) interact little, featuring only a small overlap at the pulses' edges. We can observe small deformation in the 6.84 ps image, but can only roughly conclude that the pulses propagate independently in this power region. On the other hand, intense pulses (P_0 =0.45 mJ×2) show extra behavior during the propagation

that is not described as a simple summation of two pulses. At 3.42 ps, a small peak, which is not observed in the original pulse, is created at the center between the two pulses. The peak grows during propagation ($t=5.13$ ps) and finally forms a higher peak than initial intensity distribution ($t=6.84$ ps).

Figure 4(c) shows a 3D isosurface plot corresponding to the final image ($t=6.84$ ps) in Fig. 4(b). The isosurface indicates a set of points where the intensity is equal to 6.81×10^{17} W/m^2, corresponding to 50% of the maximum power density. Additionally, a quarter of the pulse is removed for observing the cross-sectional form of the pulse. The central peak, formed around the intersection of the two pulses, shows a shadelike form that is enlarged only in the y direction. We can assign the origin of the interaction to the plasma defocusing effect from the fact that two weak light pulses ($P_0=0.30$ mJ$\times 2$) propagate independently, demonstrating the self-focusing effect with a weaker plasma defocusing effect.

IV. SUMMARY AND CONCLUSIONS

In this work, we developed a numerically stable and accurate method for numerically solving (3+1)D ENLSE beyond SVEA. Based on the Suzuki's exponential-operator expansion and space splitting of the differential operators on the discretized real space time, the developed method is an efficient method that requires calculation steps of $O(N)$ for integrating N data. Consequently, the typical elapsed time for calculating 1400-step evolution of $384\times384\times384$ data was about 11 h without a large-scale computing system. To demonstrate this method, we numerically studied the propagation phenomena of femtosecond light pulses in nitrogen gas. The calculation results were compared with the experimental results in order to establish the predictability of the present calculation for realistic phenomena. High-power phenomena of femtosecond pulses were also predicted, i.e., the multiple-cone formation and interaction of two collimated pulses in nitrogen gas. The present method is also suitable for parallel computing on cluster computing systems. Extended to large-scale calculations, this method could be applied to more complicated phenomena and has the potential to become a mediator between theoretical and experimental investigations of femtosecond-pulse propagation.

ACKNOWLEDGMENTS

The authors thank T. Hiruma, Y. Suzuki, Y. Tsuchiya, S. Aoshima, Y. Mizobuchi, and Y. Ohtake of Hamamatsu Photonics K.K. for their encouragement throughout this work. T. A. also thanks Professor K. Nakamura of Osaka City University for discussions on the general aspect of nonlinear Schrödinger equations.

[1] M. Mlejnek, E. M. Wright, and J. V. Moloney, Phys. Rev. E **58**, 4903 (1998).
[2] M. Mlejnek, M. Kolesik, J. V. Moloney, and E. M. Wright, Phys. Rev. Lett. **83**, 2938 (1999); S. L. Chin *et al.*, Appl. Phys. B **74**, 67 (2002); W. Liu *et al.*, New J. Phys. **6**, 6 (2004); G. Méchain *et al.*, Appl. Phys. B **79**, 379 (2004); G. Méchain, A. Couairon, M. Franco, B. Prade, and A. Mysyrowicz, Phys. Rev. Lett. **93**, 035003 (2004).
[3] N. Aközbek, M. Scalora, C. M. Bowden, and S. L. Chin, Opt. Commun. **191**, 353 (2001), and references therein.
[4] L. Bergé and A. Couairon, Phys. Rev. Lett. **86**, 1003 (2001).
[5] S. Tzortzakis, L. Berge, A. Couairon, M. Franco, B. Prade, and A. Mysyrowicz, Phys. Rev. Lett. **86**, 5470 (2001).
[6] A. Couairon *et al.*, J. Opt. Soc. Am. B **19**, 1117 (2002), and references therein.
[7] L. Bergé *et al.*, Phys. Rev. Lett. **92**, 225002 (2004).
[8] M. Fujimoto, S. I. Aoshima, M. Hosoda, and Y. Tsuchiya, Opt. Lett. **24**, 850 (1999); Phys. Rev. A **64**, 033813 (2001).
[9] M. Fujimoto, S. Aoshima, and Y. Tsuchiya, Opt. Lett. **27**, 309 (2002).
[10] M. Fujimoto, S. Aoshima, and Y. Tsuchiya, Meas. Sci. Technol. **13**, 1698 (2002).
[11] M. Fujimoto, Ph.D. thesis, Kyoto University, 2004 (unpublished).
[12] See, for review, A. Hasegawa, *Optical Solitons in Fibers* (Springer-Verlag, Berlin, 1989).
[13] N. Tzoar and M. Jain, Phys. Rev. A **23**, 1266 (1981).
[14] K. Okumura, Y. H. Ichikawa, and Y. Abe, Opt. Lett. **12**, 516 (1987).
[15] J. E. Rothenberg, Opt. Lett. **17**, 1340 (1992).
[16] J. K. Ranka and A. L. Gaeta, Opt. Lett. **23**, 534 (1998).
[17] T. Brabec and F. Krausz, Phys. Rev. Lett. **78**, 3282 (1997).
[18] A. A. Zozulya, S. A. Diddams, and T. S. Clement, Phys. Rev. A **58**, 3303 (1998); A. A. Zozulya, S. A. Diddams, A. G. Van Engen, and T. S. Clement, Phys. Rev. Lett. **82**, 1430 (1999).
[19] A. L. Gaeta, Phys. Rev. Lett. **84**, 3582 (2000).
[20] G. Agrawall, *Nonlinear Fiber Optics*, 2nd ed. (Academic Press, New York, 1995).
[21] H. Kumagai *et al.*, J. Opt. Soc. Am. B **20**, 597 (2002).
[22] K. Ishikawa, H. Kumagai, and K. Midorikawa, Phys. Rev. E **66**, 056608 (2002).
[23] M. Suzuki, Phys. Lett. **113**, 229 (1985).
[24] M. Suzuki, Phys. Lett. A **146**, 319 (1990).
[25] M. Suzuki, J. Math. Phys. **32**, 400 (1991).
[26] M. Suzuki, J. Math. Phys. **69**, 161 (1993).
[27] N. Watanabe and M. Tsukada, Phys. Rev. E **62**, 2914 (2000).
[28] N. Watanabe and M. Tsukada, Phys. Rev. E **65**, 036705 (2002).
[29] J. L. Richardson, Comput. Phys. Commun. **63**, 84 (1991).
[30] H. De Raedt and K. Michielsen, Comput. Phys. **8**, 600 (1994).
[31] When the light pulses are diffracted widely, e.g., in the case of the multiple-cone formation (Sec. III C), a small boundary effect is observed in the numerics around the fringe. Nevertheless, it does not produce any remarkable changes in the observed phenomena, even if the damping condition is varied.
[32] In the experiment, observations are made around the focusing position while the calculation results are shown from the origin of the z direction. A light pulse propagates a finite length be-

fore arriving at the focusing position; however, deformation of the unfocused pulse is negligible because the intensity is not enough to produce an observable nonlinear effect. This is consistent with the fact that the deformation of a weak pulse (P_0 =0.30 mJ) is small (Fig. 1). Finally, observation around the focusing position gives similar results to those calculated around the $z=0$ for collimated pulses. Strictly, the focusing condition should be taken into account as in Ref. [1], but this approach needs a large quantity of evolution steps before the initial pulse arrives at the focusing point.